Journal of Porphyrins and Phthalocyanines
J. Porphyrins Phthalocyanines 2019; **23**: 1–12
DOI: 10.1142/S1088424618501146

Published at http://www.worldscinet.com/jpp/

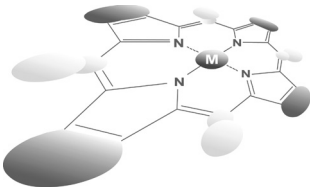

Photophysicochemical properties and photodynamic therapy activity of chloroindium(III) tetraarylporphyrins and their gold nanoparticle conjugates

Rodah C. Soy[a], Balaji Babu[a], David O. Oluwole[a], Njemuwa Nwaji[a◊◊], James Oyim[b◊◊], Edith Amuhaya[b], Earl Prinsloo[c], John Mack*[a◊] and Tebello Nyokong[a◊]

[a] *Centre for Nanotechnology Innovation, Department of Chemistry, Rhodes University, Makhanda 6140, South Africa*
[b] *School of Pharmacy and Healthy Sciences, USIU-Africa, Nairobi, Kenya*
[c] *Biotechnology Innovation Centre, Rhodes University, Makhanda 6140, South Africa*

This Paper is part of the 2019 Women in Porphyrin Science special issue.

Received 21 October 2018
Accepted 20 November 2018

ABSTRACT: Novel chloroindium(III) complexes of tetra(4-methylthiophenyl)porphyrin (**2a**) and tetra-2-thienylporphyrin (**2b**) dyes have been synthesized and characterized. The main goal of the project was to identify fully symmetric porphyrin dyes with Q-band regions that lie partially in the therapeutic window that are suitable for use in photodynamic therapy (PDT). **2a** and **2b** were found to have fluorescence quantum yield values ≤ 0.01 and moderately high singlet oxygen quantum yields (0.54–0.73) due to heavy atom effects associated with the sulfur and indium atoms. The dark toxicity and PDT activity against epithelial breast cancer cells (MCF-7) were investigated over a dose range of 3.0–40 $\mu g \cdot mL^{-1}$. The *in vitro* dark cytotoxicity of **2a** is significantly lower than that of **2b** at ≤ 40 $\mu g \cdot mL^{-1}$. **2a** was conjugated with gold nanoparticles (AuNPs) to form a nanoconjugate (**2a**-AuNPs), which exhibited a higher singlet oxygen quantum yield (Φ_Δ) value and PDT activity than was observed for **2a** alone. The results suggest that the AuNPs nanoconjugates of readily synthesized fully symmetric porphyrin dyes are potentially suitable for PDT applications, if *meso*-aryl substituents that provide scope for nanoparticle conjugation can be introduced that shift the Q bands into the therapeutic window.

KEYWORDS: porphyrins, photophysics, singlet oxygen, gold nanoparticles, photodynamic therapy, dark toxicity.

INTRODUCTION

Photodynamic therapy (PDT) has emerged as a non-invasive clinical treatment modality for cancer which is a promising alternative to conventional cancer treatment protocols such as radiotherapy, chemotherapy and surgery that are known for their harmful side effects including the indiscriminate destruction of both healthy and tumor cells [1–5]. A prerequisite requirement for PDT is a light absorbing chromophore known as a photosensitizer (PS). The technique involves the administration of a PS, which selectively targets the tumor cells, and irradiation of the PS with laser light of appropriate wavelength to initiate a series of photochemical reactions. Typically, this involves the excitation of the PS to a long-lived triplet state, which upon interaction with the intracellular molecular dioxygen subsequently results in the generation of singlet oxygen known as a reactive oxygen species (ROS) which is cytotoxic to tumor cells [1–3]. Photosensitizers intended for PDT applications should fulfil some basic requirements such as efficient generation of singlet oxygen, low dark toxicity, photostability and absorption in the near infrared therapeutic window among others [6].

Metalloporphyrin derivatives have gained considerable attention as photosensitizers in many fields such

[◊] SPP full and [◊◊] student member in good standing

*Correspondence to: John Mack, tel.: +27 46-603-7234, email: j.mack@ru.ac.za.

as in photoelectric devices, catalytic reactions, solar cells and PDT applications [6–11]. The applicability of metalloporphyrins as PS in PDT is due to their efficient photosensitization ability, particularly their ability to absorb visible light, which excites the PS to an excited singlet state, leading to intersystem crossing to the triplet manifold. Energy transfer from the lowest excited triplet state of the PS to molecular oxygen results in the generation of singlet oxygen, which is the chief cytocidal agent in the selective destruction of tumor cells [1–3]. Recently we reported the photophysicochemical properties of a Sn(IV) complex of *meso*-tetra-2-thienylporphyrin with an unusually high singlet oxygen quantum yield (Φ_Δ) value, and we demonstrated that the presence of bulky pyridyloxy axial ligands limits aggregation through π–π stacking, resulting in promising photodynamic therapy activity properties during irradiation with a 625 nm light emitting diode (LED), by enhancing the solubility of the dyes in polar solvents [12]. A significant shift of the Q_{00} band to the red relative to the analogous tetraphenylporphyrin so that it lies further into the therapeutic window also contributed to the enhanced PDT properties [12]. In this study, we extend this work to the chloroindium(III) complexes of *meso*-tetra[4-(methylthio)phenyl]porphyrin (**2a**) and *meso*-tetra-2-thienylporphyrin (**2b**). The choice of 4-(methylthio)phenyl and 2-thienyl substituents was based in part on the fact that these derivatives have been found to contain antioxidants and to exhibit antifungal, antibacterial and anticancer activity [13–16]. Incorporation of a heavy atom such as indium is also known to enhance the triplet population resulting in better singlet oxygen generation [17, 18], and the presence of axial ligands helps to prevent aggregation in aqueous solvents [12].

One of the most significant issues faced when using porphyrin dyes and their analogues in PDT is the need for selective delivery of the PS to tumor cells to avoid leaving the patient photosensitized for prolonged periods. Conjugating nanoparticles to metalloporphyrins has been found to be advantageous [19], due to their small size, high stability and high surface area, allowing for specific target localization and hence, selective accumulation in the cancer cells due to an enhanced permeability and retention (EPR) effect [19–23]. In addition, it has been established that gold nanoparticles (AuNPs) destroy tumors selectively through a photothermal effect (PTT) [21–23]. PTT is an important anticancer therapeutic strategy in which irradiation of nanoparticles embedded in the tumors with laser light results in an increase in temperature in the tumor tissues, which selectively kills cancer cells [23]. The sulfur atom in the 4-methylthiophenyl ring of **2a** enables noncovalent interactions with the AuNPs since gold is known to have a strong affinity for the electron lone pairs of sp^3 hybridized sulfur atoms [24]. The photophysicochemical properties of nanoconjugates prepared by conjugating **2a** to gold nanoparticles (**2a**-AuNPs) have been studied and their photodynamic therapy activity has been investigated.

EXPERIMENTAL

Materials

Pyrrole, 1,3-diphenylisobenzofuran (DPBF), 2-thiophenecarboxaldehyde, 4-methylthiobenzaldehyde, chloroform, methanol, petroleum ether, sodium acetate, indium(III) chloride, Trypan Blue, trypsin, ethylenediaminetetraacetic acid (EDTA) and zinc(II) tetraphenylporphyrin (ZnTPP) were purchased from Sigma-Aldrich. Dimethyl sulfoxide (DMSO) and dichloromethane were obtained from Merck. Cultures of the MCF-7 cell were obtained from Cellonex®. 10% (v/v) heat-inactivated fetal calf serum (FCS), and 100 unit·mL^{-1} penicillin-100 μg·mL^{-1} streptomycin-amphotericin B were acquired from Biowest®. Neutral red cell proliferation reagent (WST-1), Dulbecco's phosphate-buffered saline (DPBS) and Dulbecco's modified Eagle's medium (DMEM) were obtained from Lonza®. The syntheses of the chloroindium complex of 5,10,15,20-tetraphenylporphyrin (ClInTPP) [25], and free base 5,10,15,20-tetra-[4-(methylthio)-phenyl]porphyrin (H_2MTPP) [26, 27] and 5,10,15,20-tetra-2-thienylporphyrin (H_2TTP) [28, 29] were carried out as reported in the literature.

Instrumentation

Mass spectrometry data were obtained from a Bruker AutoFLEX III Smartbeam MALDI-TOF instrument, and dithranol was used as the matrix in the positive ion mode. The elemental analyses were carried out on a Vario EL III Microcube CHNS Analyzer. ^{1}H-NMR spectra were recorded on a Bruker AVANCE II 600 MHz NMR spectrometer using tetramethylsilane as the internal reference standard. X-ray diffraction (XRD) patterns were recorded on a Bruker D8 Discover diffractometer using procedures described previously [30]. The ground state electronic absorption spectra were measured on a Shimadzu UV-2550 spectrophotometer, while fluorescence excitation and emission were recorded on a Varian Eclipse spectrofluorimeter. Fluorescence lifetimes were measured using a time-correlated single photon counting setup (TCSPC) (FluoTime 300, Picoquant® GmbH) with a diode laser (LDH–P–670, Picoquant® GmbH, 20 MHz repetition rate, 44 ps pulse width) in a manner described previously [31]. The morphologies of the nanoparticles and the conjugates were assessed by transmission electron microscopy (TEM) with a Zeiss Libra model 120 operated at 100 kV. Magnetic circular dichroism (MCD) spectra [32] were recorded on a Chirascan plus spectrodichrometer equipped with a 1 tesla permanent magnet by using both the parallel and antiparallel fields and subtracting a solvent baseline.

Synthesis

The chloroindium complexes of H_2MTPP and H_2TTP were synthesized using literature methods [33, 34].

Synthesis of chloroindium(III) meso-tetra-[4-(methylthio)phenyl]porphyrin (2a). A mixture of glacial acetic acid (30 ml) and 320 mg (0.4 mmol) of H_2MTPP was stirred and brought to reflux at 100 °C. 221 mg (1.0 mmol) of $InCl_3$ and 0.6 g (7.314 mmol) sodium acetate were then added and the mixture was refluxed for a further 16 h. UV-vis absorption spectroscopy was used to monitor the completion of the reaction. The reaction mixture was cooled in ice to obtain the crude precipitate, which was filtered and washed with Millipore water (3 × 100 mL) and dried *in vacuo*. The crude product was then purified using silica gel column chromatography with chloroform/methanol (2:1) as the eluent to yield **2a** as a green-purple solid. Yield: 309 mg (96.6%). UV-vis (DMSO): λ_{max} nm (log ε) 435 (5.07), 568 (3.06), 612 (3.55). ^{1}H NMR (600 MHz, DMSO-d_6) δ 9.09–8.97 (m, 8H, Ar-H), 8.36–8.14 (m, 8H, Ar-H), 7.90–7.68 (m, 8H, Ar-H), 2.85–2.60 (m, 12H, CH_3).

Synthesis of chloroindium (III) meso-tetra-2-thienylporphyrin (2b). **2b** was synthesized in the same manner described for **2a** by using 255 mg (0.4 mmol) of H_2TTP. Yield: 249 mg (97.6%). UV-vis (DMSO): λ_{max} nm (log ε) 438 (5.50), 570 (2.51), 618 (1.88). ^{1}H NMR (600 MHz, DMSO-d_6) δ_H ppm 9.32–9.12 (m, 8H, Ar-H), 8.35–8.27 (m, 4H, Ar-H), 8.26–8.04 (m, 4H, Ar-H), 7.73–7.60 (m, 4H, Ar-H).

Conjugation of 2a to gold nanoparticles (2a-AuNPs). AuNPs were synthesized according to a reported literature method [35]. The **2a**-AuNPs nanoconjugate was synthesized by adding **2a** (10 mg, 0.01 mmol) dissolved in 5 ml of chloroform into 20 mL of refluxing toluene, followed quickly by AuNPs (4 mg) in 2 mL of toluene. After 1 h of further heating at reflux, the solution was stirred at room temperature for 24 h. The conjugate was precipitated out of solution using methanol by centrifugation for 10 min at 5000 rpm, then washed with methanol and ethanol to remove unreacted **2a**.

Photophysical parameters

Fluorescence and singlet oxygen quantum yields. The fluorescence quantum yield (Φ_F) values for ClInTPP, **2a**, **2b** and the **2a**-AuNPs nanoconjugate were determined in DMSO using a comparative method described previously in the literature [36]. Zinc(II) *meso*-substituted tetraphenylporphyrin (ZnTPP) was used as the standard (Φ_F = 0.0397) [36]. The singlet oxygen quantum yield (Φ_Δ) values were also calculated using a comparative method [37, 38] by using DPBF as a singlet oxygen quencher in DMSO and Rose Bengal as the standard (Φ_Δ = 0.76) [39].

Theoretical calculations. Geometry optimizations of the structures of the ClInTPP parent porphyrin complex, **2a** and **2b** were carried with the Gaussian 09 software package [40] using the B3LYP functional with SDD basis sets. The optimized B3LYP geometries were then used to carry out TD-DFT calculations with the CAM-B3LYP functional and SDD basis sets, since the CAM-B3LYP functional is known to provide more accurate results for transitions with significant charge transfer properties [41].

In vitro dark cytotoxicity and PDT activity. *In vitro* PDT studies were conducted using the illumination kit of a Modulight® 7710−680 Medical Laser fitted with a Thorlab M625L3 light emitting dioide that was found to provide an irradiance of 240 $mW \cdot cm^{-2}$ (measured with a Coherent FieldmaxII TOP energy/power meter fitted with a Coherent Powermax PM10 sensor), to illuminate a 127.76 × 85.48 mm 96 well tissue culture plate. The culturing of the MCF-7 cancer cell line was carried out as described in the literature [42, 43]. The MCF-7 cells were cultured using Dulbecco's modified Eagles' medium (DMEM) containing 4.5 $g \cdot L^{-1}$ glucose with L-glutamine and phenol red, supplemented with 10% (v/v) heat-inactivated fetal calf serum (FCS) and 5% 100 unit mL^{-1} penicillin 100 $\mu g \cdot mL^{-1}$ streptomycin amphotericin B. The cells were grown in a 25 cm^2 vented flask (Porvair) and incubated in a humidified 5% CO_2 atmosphere at 37 °C until 70% confluence was achieved. Standard trypsinization and cell seeding were undertaken as described in the literature [42, 43]. Doses of **2a**, **2a**-AuNPs and **2b** were administered over a concentration range of 3–40 $\mu g \cdot mL^{-1}$ by adding appropriate aliquots of stock solution prepared by dissolving the drugs in DMSO and making up the volume with supplemented DMEM as described in literature [42, 43]. No irradiation was performed on the treated cells for the *in vitro* dark cytotoxicity studies while the PDT study involved 10 min irradiation with the Thorlabs LED at 625 nm. A Zeiss AxioVert.A1 Fluorescence LED inverted microscope was used for routine examination of the cells. After 24 h of drug treatment, the cells were washed with 100 μL DPBS and re-incubated in fresh culture media. Post-treatment cell viability was measured using the cell proliferation neutral red reagent (WST-1 assay) on a Synergy 2 multi-mode microplate reader (BioTek®) at a wavelength of 450 nm. The percentage cell viability was determined as a function of absorbance sample (drug treated) over absorbance control (culture media only); both determined at 450 nm. This is described in Equation 1:

$$\%\ \text{Cell Viability} = \frac{\text{Absorbance of samples at 450 nm}}{\text{Absorbance of control at 450 nm}} \times 100 \quad (1)$$

The experimental data obtained for *in vitro* and photodynamic therapy studies were analyzed statistically. Each experiment was carried out in triplicate, and the analysis of variance (ANOVA) was evaluated for the *in vitro* and photodynamic therapy data of the drugs against MCF-7 cell line.

RESULTS AND DISCUSSION

Synthesis and characterization of 2a and 2b

Scheme 1 provides the synthetic routes for **2a** and **2b**. The complexes were characterized using UV-vis and ^{1}H-NMR spectroscopy, elemental analysis and MALDI-TOF mass spectrometry. The results obtained were in close agreement with the proposed structures. The ^{1}H-NMR spectrum of **2a** has methyl proton peaks from the *meso*-aryl substituents at 2.77 and 2.09 ppm, which afforded 12 protons upon integration, while the aromatic ring proton peaks for **2a** and **2b** lie in the 7.6–9.2 ppm region and integrate to the expected number of protons.

Electronic absorption spectra of 2a and 2b

The π-MOs associated with the 16 atom 18 π-electron inner ligand perimeter are arranged in an $M_L = 0, \pm1, \pm2, \pm3, \pm4, \pm5, \pm6, \pm7, 8$ sequence in ascending energy terms due to the angular nodal properties associated with the porphyrin ring. Since the HOMO and LUMO have M_L values of ±4 and ±5, there are four and five angular nodal planes (Fig. 1), respectively. Gouterman's 4-orbital model [44] predicts the presence an allowed B transition ($\Delta M_L = \pm1$) at high energy and a forbidden Q transition ($\Delta M_L = \pm9$) at lower energy on this basis. In order to facilitate a comparison of the MOs of different complexes, Michl [45] referred to π-MOs with angular nodal planes that lie on the *y*-axis as the **a** and **-a** MOs, respectively, while the corresponding MOs that have significant MO coefficients on the *y*-axis are referred to as the **s** and **-s** MOs (Fig. 1). The introduction of different *meso*-aryl groups to form **2a** and **2b** makes only relatively minor changes to the electronic structure of the parent ClInTPP complex. A stabilization is predicted for the frontier π-MOs of **2a** and **2b** relative to those of ClInTPP. The smaller average HOMO–LUMO gap of **2b** when all four frontier π-MOs

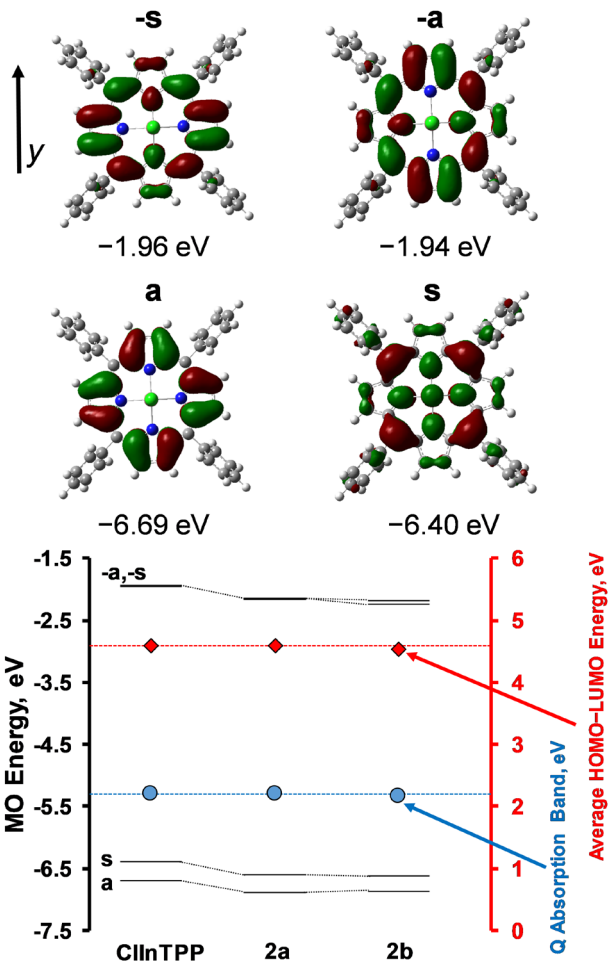

Fig. 1. Angular nodal patterns of the **a**, **s**, **-a** and **-s** MOs of the parent ClInTPP complex (TOP). MO energies of ClInTPP, **2a** and **2b** (BOTTOM). The HOMO–LUMO gap energies and the energy of the Q_{00} band are highlighted with red diamonds and blue circles are plotted against the secondary axis

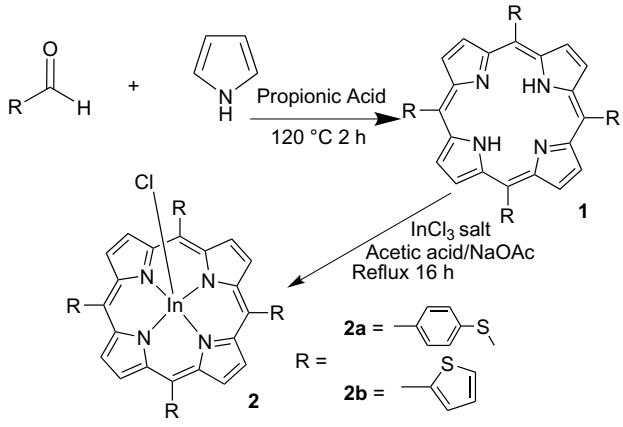

Scheme 1. The synthetic pathway for chloroindium (III) complexes of tetra(4-methylthio)phenylporphyrin (**2a**) and tetra-2-thienylporphyrin (**2b**)

are taken into account arises primarily from there being a larger stabilization of the **-a** and **-s** MOs and this makes this dye potentially more suitable for use in PDT since there is greater absorption in the therapeutic window.

The UV-vis absorption spectra of **2a** and **2b** (Fig. 2) in DMSO are typical of metalloporphyrin spectra with four-fold symmetry and are characterized by an intense B (or Soret) band in the 400–450 nm region and weaker Q_{00} and Q_{01} bands further to the red for porphyrin complexes [46]. The B band for **2a** is observed at 435 nm, and the two Q bands lie at 567 and 607 nm, while for **2b**, these bands are observed at 439, 573 and 618 nm, respectively. There is a consistent red shift of the bands observed for **2b** relative to those of **2a**, due to the differing effects of the *meso*-aryl substituents on the HOMO–LUMO gap (Fig. 1). This has been attributed to the smaller size of the *meso*-2-thienyl groups when compared to six-membered phenyl rings [47, 48]. The fluorescence emission spectra of **2a** and **2b** in DMSO are shown as insets in Fig. 2. The emission spectra are typical of metalloporphyrins with

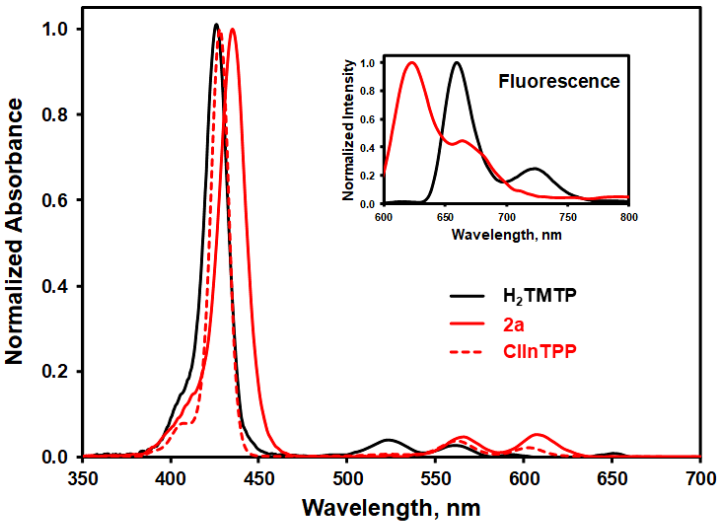

(a)

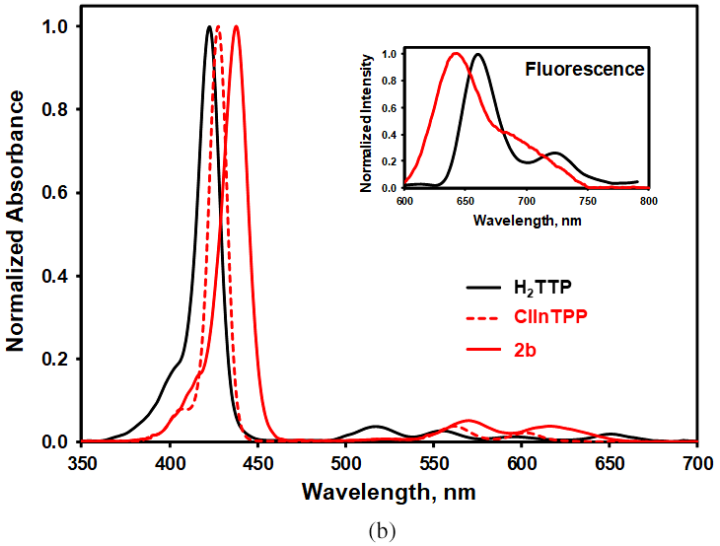

(b)

Fig. 2. UV-vis absorption spectra of (a) H_2MTPP, **2a** and ClInTPP, (b) H_2TTP, **2b** and ClInTPP in DMSO. Fluorescence spectra are provided as insets with the same line types used as for the absorption spectra

two bands of different intensities [49]. For **2a**, the bands were observed at 625 and 670 nm, while those of **2b** are observed at 643 and 689 nm. In a similar manner to the absorption spectra, the fluorescence emission bands for **2b** are hence shifted to longer wavelengths.

TD-DFT calculations were carried out to analyze the trends in the electronic structures and optical spectra of **2a** and **2b** (Fig. 3 and Table 1). The trends observed in the calculated spectra are similar to those in the experimental data, but there is a significantly smaller red shift predicted for **2a** relative to the parent In ClTPP complex than was observed experimentally. This may be related to there being a fixed geometry for the freely rotating *meso*-aryl substituents in the calculations, which results in an inaccurate prediction of their mesomeric effects on the frontier MOs that are localized primarily on the inner perimeter of the porphyrin ring. MCD spectroscopy has proven to be an important technique for identifying the electronic structures and state degeneracies of porphyrins and related macrocycles, which cannot be obtained from UV-vis absorption spectroscopy alone [50, 51]. The MCD spectra of the complexes showed cross-over points between the negative and positive lobes of intensity at 564 nm and 607 nm for **2a** and 574 nm and 618 nm for **2b**, essentially corresponding to the Q-band maxima observed in corresponding UV-vis absorption spectra (Fig. 3). This is the pattern that would normally be anticipated for the Faraday $\mathcal{A}_1$ terms associated with the main transitions of metal porphyrins with four-fold symmetry, since the derivative shaped signals arise from the Zeeman splitting of the orbitally degenerate excited states that are predicted in the TD-DFT calculations (Table 1) for the Q and B transitions [32, 51].

Synthesis and characterization of AuNPs and the 2a-AuNPs nanoconjugate

Scheme 2 illustrates the synthetic route for conjugation of AuNPs to complex **2a**. The linkage of nanoparticles to the surface of **2a** is expected to occur *via* non-covalent Au–S interactions due to the high affinity of these atoms [23]. Porphyrins are approximately 1 nm in diameter; hence, it is likely that more than one porphyrin will be bonded onto the surface of AuNPs (*ca.* 16 nm). The number of porphyrins bonded to the AuNPs was estimated according to the reported literature methods using absorption instead of fluorescence [52]. This involves comparing the absorbance intensity of the Q bands of the porphyrin in the conjugate with that of the porphyrin before conjugation [53]. The loading of porphyrins (Ps) to the nanoparticles (NPs) in μg (P)/mg (NP) was determined to be 30 on this basis.

Electronic absorption spectra of 2a-AuNPs

The UV-vis absorption spectra of the AuNPs alone, **2a** and its nanoconjugate (**2a**-AuNPs) are shown in Fig. 4. The surface plasmon resonance (SPR) band of the AuNPs was observed at 536 nm. However, upon conjugation of **2a** to the AuNPs, the shoulder of intensity arising from the SPR band was observed at 523 nm, thus indicating an apparent blue shift. The absorption spectra of **2a-**AuNPs nanoconjugate showed a significant blue shift of 6 nm of the B band to 429 nm when compared to that of **2a** at 435 nm (Table 2). This could be due to close packing attributed to the orientation of metalloporphyrins on the surface of the nanoparticles [53–56]. A typical

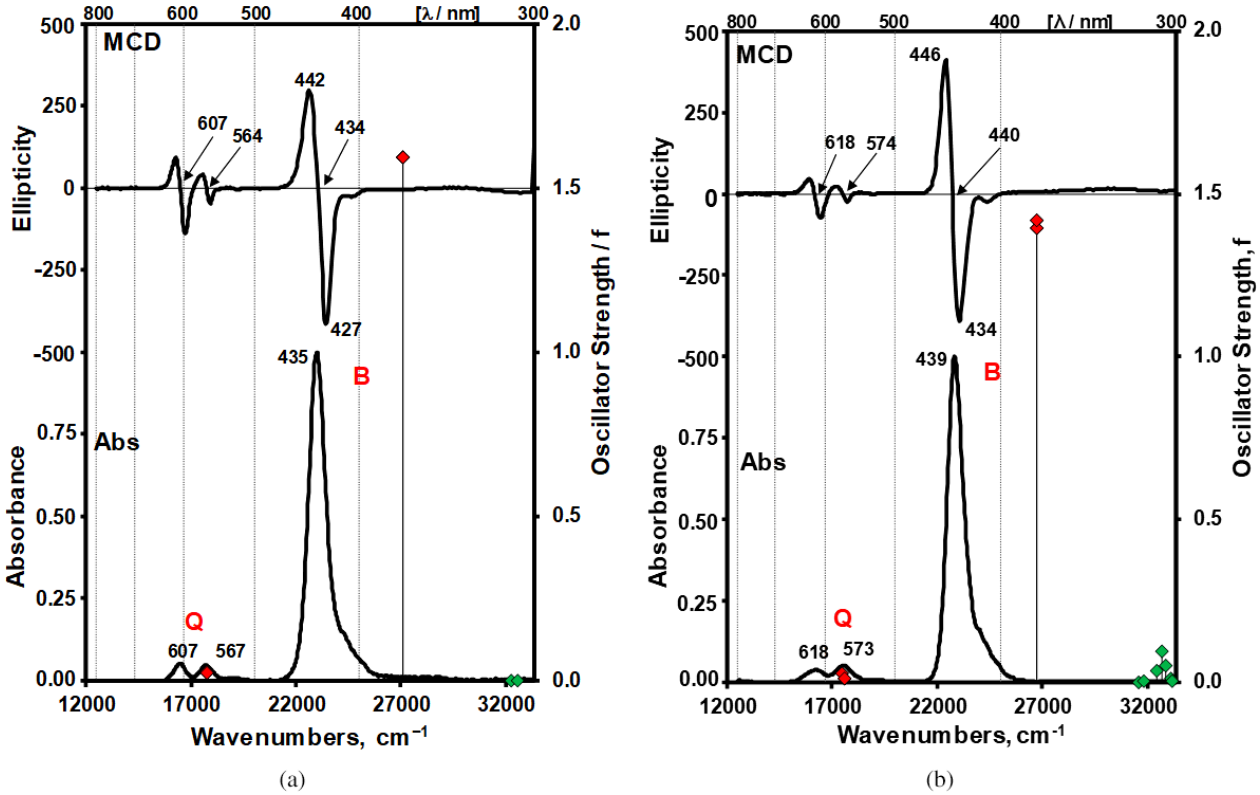

Fig. 3. Absorption and MCD spectra of **2a** (a) and **2b** (b) in DMSO. The calculated TD-DFT spectra of **2a** and **2b** plotted against secondary axis. The red diamonds highlight the Q and B bands associated with Gouterman's 4-orbital model [44]. The details of calculations are provided in Table 1

Table 1. Calculated UV-vis absorption spectra of the B3LYP optimized geometries of the parent ClInTPP complex, **2a** and **2b** obtained using the CAM-B3LYP functional with SDD basis set

				ClInTPP			
Band[a]	**#**[b]		**Calc**[c]		**Exp**[d]		**Wavefunction**[e] =
—	**1**	—	—	—	—	—	Ground state
Q	**2,3**	17.8	563	(0.02)	16.6	603	**60% s → -a/-s; 40% a → -a/-s;** …
B	**4,5**	26.2	367	(1.43)	23.4	428	**60% a → -a/-s; 40% s → -a/-s;** …
				2a			
—	**1**	—	—	—	—	—	Ground state
Q	**2,3**	17.7	564	(0.03)	16.3	612	**60% s → -a/-s; 40% a → -a/-s;** …
B	**4,5**	27.1	369	(1.59)	23.0	435	**59% a → -a/-s; 40% s → -a/-s;** …
				2b			
—	**1**	—	—	—	—	—	Ground state
Q	**2,3**	17.5	572	(0.03)	16.2	618	**59% s → -a/-s; 40% a → -a/-s;** …
B	**4,5**	26.7	374	(1.40)	22.8	438	**58% a → -a/-s; 38% s → -a/-s;** …

[a] Band assignment described in the text. [b] The number of the state assigned in terms of ascending energy within the TD-DFT calculation. [c] Calculated band energies ($10^3 \cdot cm^{-1}$), wavelengths (nm) and oscillator strengths in parentheses (f). [d] Observed energies ($10^3 \cdot cm^{-1}$) and wavelengths (nm), [e] The wave functions based on the eigenvectors predicted by TD-DFT. One-electron transitions associated with the **a**, **s**, **-a** and **-s** MOs are highlighted in bold.

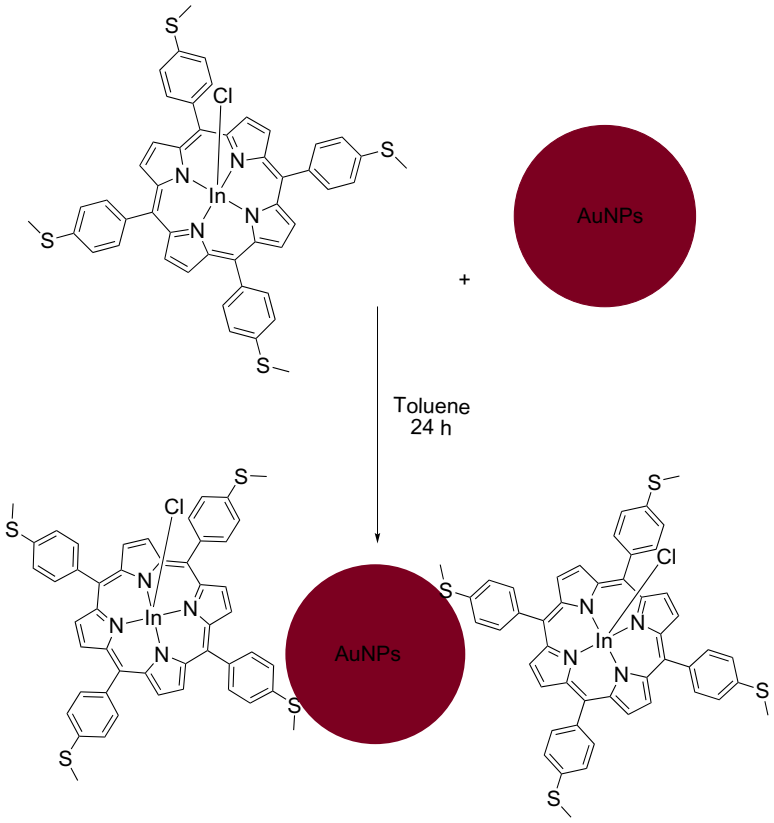

Scheme 2. The synthetic pathway for **2a**-AuNPs

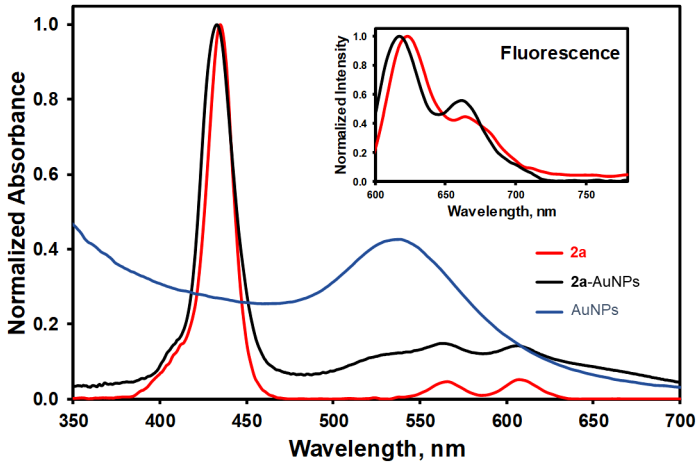

Fig. 4. Absorption spectra of **2a**-AuNPs (black) and **2a** (red) and AuNPs (blue) in DMSO. Fluorescence spectra are provided as an inset with the same line types used as for the absorption spectra

metalloporphyrin fluorescence emission spectrum was observed for the **2a-**AuNPs conjugate (Fig. 4 insert) with bands at 617 and 662 nm. There is a 9 nm blue shift of the emission bands relative to those in the spectrum of **2a**.

Transmission electron microscopy

The TEM micrographs of AuNPs and the **2a**-AuNPs nanoconjugate are shown in Fig. 5. The AuNPs were monodispersed, and the average size was *ca.* 16 nm. Upon conjugation to form **2a**-AuNPs, aggregation was observed, and there was an increase in the average size to 26 nm. This can be attributed to the interactions of metalloporphyrins on adjacent nanoparticles *via* π–π stacking [55].

X-ray diffraction

The X-ray diffraction (XRD) patterns of the AuNPs, **2a** and **2a**-AuNPs nanoconjugate are shown in Fig. 6.

Table 2. The photophysicochemical parameters of **2a**, **2b** and **2a**-AuNPs conjugate in DMSO

	λ_{Abs} (nm)			SPR	Size[a] (nm)	P loading (μg/mg)	λ_{em} (nm)	Φ_F	τ_F (ns)	Φ_Δ
	B	Q_{01}	Q_{00}							
2a	435	566	607	—	—	—	625	0.010	0.51	0.54
2b	438	573	618	—	—	—	643	0.007	0.44	0.73
ClInTPP	428	561	601	—	—	—	646	0.05[a]	0.8[a]	0.72[a]
AuNPs	—	—	—	536	16	—	—	—	—	—
2a-AuNPs	429	573	618	523	26	30	617	0.005	0.41	0.63

[a]Value from Ref. 47.

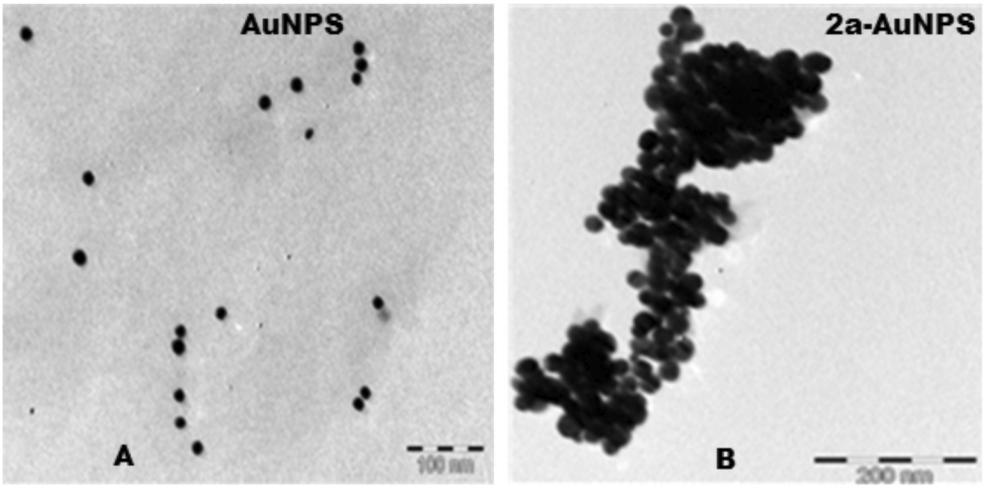

Fig. 5. Representative TEM micrographs of (a) AuNPs and (b) **2a**-AuNPs

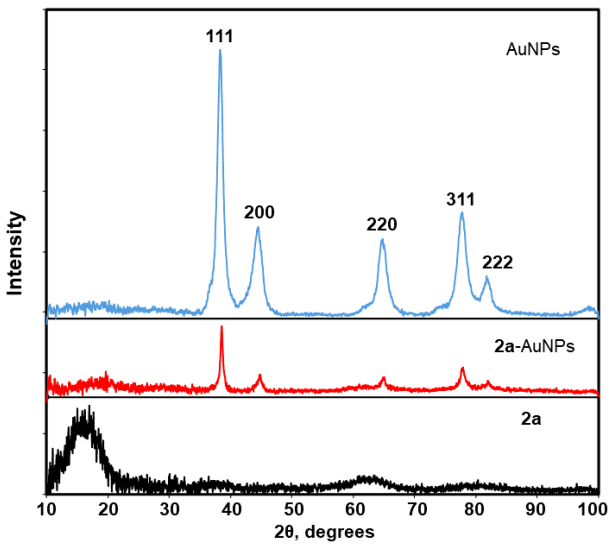

Fig. 6. XRD diffractograms of **2a**, **2a**-AuNPs, and AuNPs

The XRD diffraction patterns for AuNPs showed well-defined crystalline peaks which correspond to 111, 200, 220, 311, and 222 planes of the face centered-cubic structures of metallic gold [57]. Peak broadening was observed for **2a** between 10 and 20° as would normally be anticipated for amorphous porphyrin samples [57]. A similar peak broadening is observed between 10 and 20° for **2a**-AuNPs along with the presence of the crystalline peaks corresponding to AuNPs that are consistent with the formation of a nanoconjugate.

Fluorescence quantum yields and lifetimes

Table 2 provides a summary of the photophysicochemical parameters of **2a**, **2b**, the parent ClInTPP porphyrin complex and the **2a-**AuNPs conjugate. The fluorescence quantum yield and lifetime (τ_F) values were measured in DMSO. A lower Φ_F value was obtained for **2b** than for **2a** (Table 2). This can be attributed to the

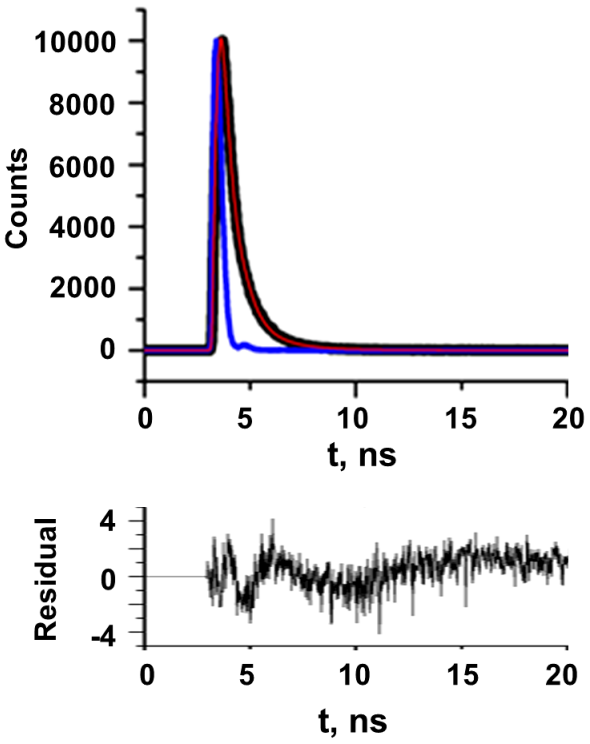

Fig. 7. Representative fluorescence decay (black), χ^2 fitting (red) and instrumental response function (blue) of **2a** in DMSO

meso-2-thienyl substituents which enhance the rate of intersystem crossing to the triplet manifold due to the presence of sulfur atoms [28, 29]. Upon conjugation of **2a** to the AuNPs a further decrease in the Φ_F value was observed (Table 2). This is probably due to the deactivation of the singlet excited state of **2a** by the AuNPs due to the external heavy atom effect, hence, enhancing the rate of intersystem crossing to the triplet state [58]. A typical fluorescence decay curve for **2a** is shown in Fig. 7. Mono-exponential curves were used to derive the τ_F values for **2a** and **2b**. **2b** was found to have a shorter lifetime than **2a** (Table 2). In contrast, a biexponential decay curve was observed for the **2a**-AuNPs nanoconjugate. An average lifetime is provided in Table 2, which is shorter than that of **2a** alone. The biexponential fluorescence decay could be due to the presence of different orientations of **2a** with respect to the nanoparticles, which results in differing interactions between the fluorophore and the free electrons of the metallic surface [59]. This alters the electric field around the molecules and may result in a decrease or increase in fluorescence lifetimes depending on the distance between and the relative orientations of the molecules and metallic nanoparticles [54, 59]. These data suggest that the observed reduction in the Φ_F and τ_F values following conjugation of **2a** is related to external heavy atom effect from the AuNPs [60].

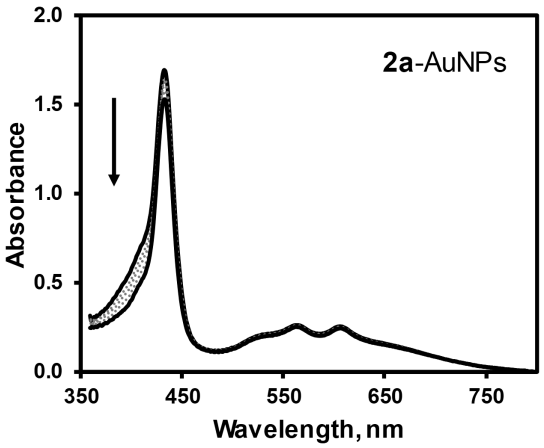

Fig. 8. Representative spectra for **2a**-AuNPs in DMSO during the determination of the Φ_Δ value with DPBF as a scavenger

Singlet oxygen quantum yields

Singlet oxygen is produced through an energy transfer process between the excited triplet state of the PS and ground state molecular oxygen [9]. In this study, the Φ_Δ value was determined by monitoring the chemical photodegradation of DPBF as a singlet oxygen quencher in DMSO. Figure 8 shows the spectral changes observed for the **2a**-AuNPs nanoconjugate. The Φ_Δ values ranging from 0.54 for **2a** to 0.73 for **2b** (Table 2) reflect the very low Φ_F values of 0.010 for **2a** and 0.007 for **2b**, due to the enhanced rate of intersystem crossing related to the presence of the central In(III) ion. This, in turn, increases the interaction between ground state molecular dioxygen with the excited triplet state of the photosensitizer. There is an increase in the Φ_Δ value of **2a**-AuNPs compared to that of **2a** as would be anticipated based on an external heavy atom effect [60].

Cell studies

In vitro dark cytotoxicity. *In vitro* dark cytotoxicity investigations were carried out for **2a**, **2b** and the **2a**-AuNPs conjugate using a range of concentrations from 3.0–40 $\mu g \cdot mL^{-1}$. Histograms showing the PS concentrations against percentage cell viability are shown in Fig. 9. The photosensitizers considered in this study showed over 50% cell viability at 3.0–20 $\mu g \cdot mL^{-1}$, suggesting that they were relatively innocuous against MCF-7 breast cancer cells in the absence of irradiation. The *in vitro* dark cytotoxicity of **2a** and its **2a**-AuNPs nanoconjugate showed minimal cytotoxicity when compared to **2b** at ≤ 40 $\mu g \cdot mL^{-1}$ (Fig. 10). Treatment with **2a** resulted in cell viabilities $\geq 67\%$ at ≤ 40 $\mu g \cdot mL^{-1}$ while **2a**-AuNPs exhibited cell viabilities $\geq 89\%$ and **2b** showed a slight cytotoxic effect with a cell viability value of 49% at 40 $\mu g \cdot mL^{-1}$. This suggests that the

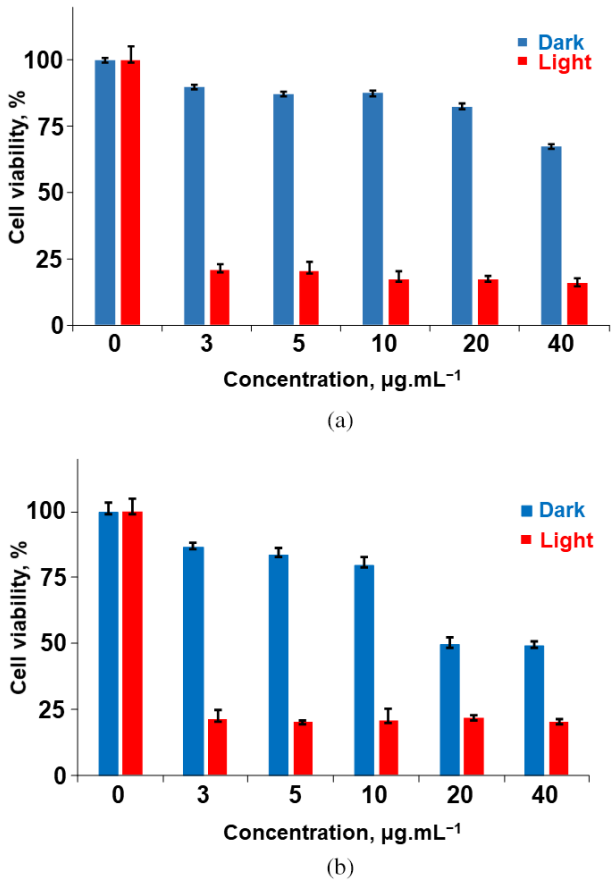

Fig. 9. Histograms showing percentage cell viability in the dark and after irradiation of (a) **2a** and (b) **2b**

conjugation of **2a** to AuNPs reduces the dark cytotoxicity significantly at higher concentrations. Essentially, low cell viability indicates higher dark cytotoxicity, which is an undesirable feature for the PDT application since the photosensitizer should only be cytotoxic in the presence of light [9].

Photodynamic therapy activity. The investigation of the PDT activities of **2a**, **2b** and the **2a**-AuNPs conjugate was carried out over the same range of concentrations (3.0–40 $\mu g \cdot mL^{-1}$) that was used for the dark toxicity studies and involved excitation with a Thorlabs 625 nm LED for 10 min (625 nm, dose of 144 $J \cdot cm^{-2}$). Treatment with **2a** resulted in greater than 79% cell death at ≤ 40 $\mu g \cdot mL^{-1}$, while the use of **2a**-AuNPs nanoconjugate and **2b** resulted in ≥ 89% and ≥ 82% cell death, respectively (Fig. 10). Overall, the PDT activity of the **2a**-AuNPs nanoconjugate outperformed that of **2a** as would be anticipated based on the higher Φ_Δ value (Table 2).

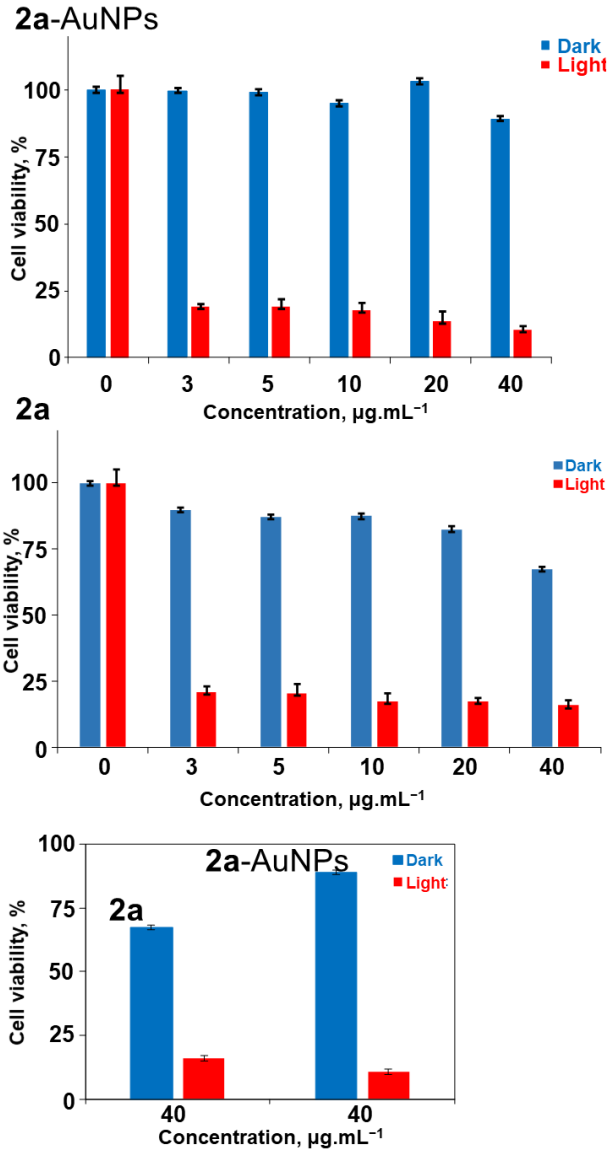

Fig. 10. Histograms showing percentage cell viability in the dark and after irradiation of **2a**-AuNPs (TOP) and **2a** (CENTER), and a comparison of the values obtained at 40 $\mu g \cdot mL^{-1}$. (BOTTOM)

CONCLUSION

In this work, the chloroindium(III) complexes of tetra(4-methylthiophenyl)porphyrin and tetra-2-thienyl-porphyrin have been successfully synthesized and characterized along with the AuNPs nanoconjugate of the former. Although **2b** has a higher Φ_Δ value, significant dark toxicity is observed during cell studies with the MCF-7 cancer cell line. **2a** exhibits an enhanced Φ_Δ value upon conjugation to AuNPs, and improved dark cytotoxicity and phototoxicity properties are also observed in this context. These results demonstrate the potential utility of the **2a**-AuNPs nanoconjugate for application in PDT, since the nanoparticles also enhance the delivery of the photosensitizer dye and its selective accumulation in cancer tumors due to enhanced solubility in aqueous solvents and the EPR effect.

Acknowledgment

This work was supported by National Research Foundation (NRF) of South Africa SA-Kenya collaborative

grant (UID: 105809) to JM and EA, the Department of Science and Technology (DST) Nanotechnology (NIC)/NRF) of South Africa through DST/NRF South African Research Chairs Initiative to Professor of Medicinal Chemistry and Nanotechnology (UID: 62620), Rhodes University and the Organization for Women in Science for the Developing World (OWSD) scholarship to RS. The theoretical calculations were carried out at the Centre for High Performance Computing in Cape Town.

REFERENCES

1. Zhang J, Jiang C, Longo JP, Azevedo RB, Zhang H and Muehlmann LA. *Acta Pharm. Sin. B*. 2018; **8**: 137–146.
2. Abrahamse H and Hamblin MR. *Biochem. J*. 2016; **473**: 347–364.
3. Henderson BW and Dougherty T. *J. Photochem. Photobiol.* 1992; **55**: 145–157.
4. Agostinis P, Berg K, Cengel KA, Foster TH, Girotti AW, Gollnick SO, Hahn SM, Hamblin MR, Juzeniene A, Kessel D and Korbelik M. *CA: Cancer J. Clin*. 2011; **61**: 250–281.
5. Managa M, Britton J, Prinsloo E and Nyokong T. *J. Coord. Chem*. 2016; **69**: 3491–3506.
6. Ethirajan M, Chen Y, Joshi PK and Pandey RK. *Chem. Soc. Rev*. 2011, **40**: 340–362.
7. *The Porphyrin Handbook*, *Vol.* 3, Kadish KM, Smith KM and Guilard R. (Eds.), Elsevier; 2000.
8. Sternberg ED, Dolphin D and Brückner C. *Tetrahedron* 1998; **54**: 4151–4202.
9. Long J, Xu J, Yang Y, Wen J and Jia C. *Mater. Sci. Eng. B* 2011; **176**: 1271–1276.
10. Li LL and Diau EW. *Chem. Soc. Rev.* 2013; **42**: 291–304.
11. Ryabova V, Schulte A, Erichsen T and Schuhmann W. *Analyst* 2005; **130**: 1245–1252.
12. Babu B, Amuhaya E, Oluwole DO, Prinsloo E, Mack J and Nyokong T. *Med. Chem. Commun.* 2018, in press (DOI: 10.1039/C8MD00373D).
13. Ashok M, Holla BS and Kumari NS. *Eur. J. Med. Chem*. 2007; **42**: 380–385.
14. Dos Santos FA, Pereira MC, de Oliveira TB, Mendonça Junior FJ, de Lima MD, Pitta MG, Pitta ID, de Melo R, Barreto MJ, da Rocha P and Galdino M. *Anticancer Drugs* 2018; **29**: 157–166.
15. Lan L, Qin W, Zhan X, Liu Z and Mao Z. *Anticancer Agents Med. Chem*. 2014; **14**: 994–1002.
16. El-Nakkady SS, Abbas SE, Roaiah HM and Ali IH. *Global J. Pharm*. 2012; **6**: 166–177.
17. Solov'ev KN and Borisevich EA. *Phys.-Usp*. 2005; **48**: 231–253.
18. Azenha EG, Serra AC, Pineiro M, Pereira MM, de Melo JS, Arnaut LG, Formosinho SJ and Gonsalves AMd'AR. *Chem. Phys*. 2002; **280**: 177–190.
19. (a) Peer D, Karp JM, Hong S, Farokhzad OC, Margalit R and Langer R. *Nat. Nanotech.* 2007; **2**: 751–760. (b) Shao S, Rajendiran V and Lovell JF. *Coord. Chem. Rev*. 2019; **379**: 99–120. (c) Mauriello Jimenez C, Aggad D, Croissant JG, Tresfield K, Laurencin D, Berthomieu D, Cubedo N, Rossel M, Alsaiari S, Anjum DH and Sougrat R. *Adv. Funct. Mater.* 2018, **28**: 1800235. (d) Zhang Y and Lovell JF. *Theranostics* 2012; **2**: 905–915. (e) Wang J, Zhong Y, Wang X, Yang W, Bai F, Zhang B, Alarid L, Bian K and Fan H. *Nano Lett*. 2017; **7**: 6916–6921.
20. Jaque D, Maestro LM, Del Rosal B, Haro-Gonzalez P, Benayas A, Plaza JL, Rodriguez EM and Sole JG. *Nanoscale* 2014; **6**: 9494–9530.
21. Sano K, Nakajima T, Choyke PL and Kobayashi H. *ACS Nano*. 2012; **7**: 717–724.
22. Li JL and Gu M. *IEEE J. Sel. Top. Quantum Electron*. 2010; **16**: 989–996.
23. Riley RS and Day ES. *Wiley Interdiscip. Rev. Nanomed. Nanobiotechnol*. 2017; **9**: e1449/1–e1449/16.
24. Pensa E, Cortes E, Corthey G, Carro P, Vericat C, Fonticelli MH, Benitez G, Rubert AA and Salvarezza RC. *Acc. Chem. Res*. 2012; **45**: 1183–1192.
25. Silva AR, Pelegrino AC, Tedesco AC and Jorge RA. *J. Braz. Chem. Soc*. 2008; **19**: 491–501.
26. Nia S, Gong X, Drain CM, Jurow M, Rizvi W and Qureshy M. *J. Porphyrins Phthalocyanines* 2010; **14**: 621–629.
27. Johnstone RA, Nunes ML, Pereira MM, Gonsalves AM and Serra AC. *Heterocycles* 1996; **7**: 1423–1437.
28. Gupta I, Hung CH and Ravikanth M. *Eur. J. Org. Chem*. 2003; 4392–4400.
29. Ghosh A, Mobin SM, Fröhlich R, Butcher RJ, Maity DK and Ravikanth M. *Inorg. Chem.* 2010; **49**: 8287–8297.
30. Masilela N and Nyokong T. *J. Photochem. Photobiol. A*. 2011; **223**: 124–131.
31. Modisha P, Antunes E, Mack J and Nyokong T. *Int. J. Nanosci.* 2013; **12**: 1350010.
32. Mack J and Kobayashi N. *Recent Applications of MCD Spectroscopy to Porphyrinoids.* In *Multiporphyrin Arrays*, 2011, pp. 91–147.
33. Hong TN, Sheu YH, Jang KW, Chen JH, Wang SS, Wang JC and Wang SL. *Polyhedron* 1996; **15**: 2647–2654.
34. Bajju GD, Ahmed A, Gupta D, Kapahi A and Devi G. *Bioinorg. Chem. Appl*. 2014; 865407/1–865407/7.
35. Hiramatsu H and Osterloh FE. *Chem. Mater.* 2004; **16**: 2509–2511.
36. Zhao Z, Nyokong T and Maree MD. *Dalton Trans*. 2005, **23**: 3732–3737.
37. Spiller W, Kliesch H, Wöhrle D, Hackbarth S, Röder B and Schnurpfeil G. *J. Porphyrins Phthalocyanines* 1998; **2**: 145–158.
38. Redmond RW and Gamlin JN. *Photochem. Photobiol.* 1999; **70**: 391–475.

39. Gandra N, Frank AT, Le Gendre O, Sawwan N, Aebisher D, Liebman JF, Houk KN, Greer A and Gao R. *Tetrahedron* 2006; **62**: 10771–10776.
40. Gaussian 09, Revision E.01, Frisch MJ, Trucks GW, Schlegel HB, Scuseria GE, Robb MA, Cheeseman JR, Scalmani G, Barone V, Mennucci B, Petersson GA, Nakatsuji H, Caricato M, Li X, Hratchian HP, Izmaylov AF, Bloino J, Zheng G, Sonnenberg JL, Hada M, Ehara M, Toyota K, Fukuda R, Hasegawa J, Ishida M, Nakajima T, Honda Y, Kitao O, Nakai H, Vreven T, Montgomery Jr. JA, Peralta JE, Ogliaro F, Bearpark M, Heyd JJ, Brothers E, Kudin KN, Staroverov VN, Kobayashi R, Normand J, Raghavachari K, Rendell A, Burant JC, Iyengar SS, Tomasi J, Cossi M, Rega N, Millam JM, Klene M, Knox JE, Cross JB, Bakken V, Adamo C, Jaramillo J, Gomperts R, Stratmann RE, Yazyev O, Austin AJ, Cammi R, Pomelli C, Ochterski JW, Martin RL, Morokuma K, Zakrzewski VG, Voth GA, Salvador P, Dannenberg JJ, Dapprich S, Daniels AD, Farkas Ö, Foresman JB, Ortiz JV, Cioslowski J and Fox DJ. Gaussian, Inc., Wallingford CT, 2009.
41. Magyar RJ and Tretiak S. *J. Chem. Theory Comp*. 2007; **3**: 976–987.
42. Oluwole DO, Prinsloo E and Nyokong T. *Spectrochim. Acta A* 2017; **173**: 292–300.
43. Oluwole DO, Prinsloo E and Nyokong T. *Polyhedron* 2016; **119**: 434–444.
44. Gouterman M. In *The Porphyrins*, *Vol III*, *Part A*, Dolphin D. (Ed.), Academic Press: New York, 1978, pp. 1–165.
45. Michl J. *Tetrahedron* 1984; **40**: 3845–3924.
46. Huang X, Nakanishi K and Berova N. *Chirality* 2000; **12**: 237–255.
47. da Silva AR, Inada NM, Rettori D, Baratti MO, Vercesi AE and Jorge RA. *J. Photochem. Photobiol. B* 2009; **94**: 101–112.
48. (a) Brückner C, Foss PC, Sullivan JO, Pelto R, Zeller M, Birge RR and Crundwell G. *Phys. Chem. Chem. Phys*. 2006; **8**: 2402–2412. (b) Gupta I and Ravikanth M. *J. Photochem. Photobiol. A* 2006; **177**: 156–163.
49. Uttamlal M and Holmes-Smith AS. *Chem. Phys. Lett*. 2008; **454**: 223–228.
50. Mack J. *Chem. Rev.* 2017; **117**: 3444–3478.
51. Mack J, Stillman MJ and Kobayashi N. *Coord. Chem. Rev.* 2007; **251**: 429–453.
52. Chandrasekharan N, Kamat PV, Hu J and Jones G. *J. Phys. Chem. B* 2000; **104**: 11103–11109.
53. Nwaji N, Mack J and Nyokong T. *Opt. Mater*. 2018; **82**: 93–103.
54. Thomas S, Nair SK, Jamal EM, Al-Harthi SH, Varma MR and Anantharaman MR. *Nanotechnology* 2008; **19**: 075710.
55. Lee KS and El-Sayed MA. *J. Phys. Chem. B* 2006; **110**: 19220–19225.
56. Ara MM, Dehghani Z, Sahraei R, Daneshfar A, Javadi Z and Divsar F. *J. Quant. Spectrosc. Radiat. Transfer* 2012; **113**: 366–372.
57. (a) Byrn MP, Curtis CJ, Hsiou Y, Khan SI, Sawin PA, Tendick SK, Terzis A and Strouse CE. *J. Am. Chem. Soc*. 1993; **115**: 9480–9497. (b) Smithery DW, Wilson SR and Suslick KS. *Inorg. Chem.* 2003; **42**: 7719–7721. (c) Huijser A, Suijkerbuijk BM, Klein Gebbink RJ, Savenije TJ and Siebbeles LD. *J. Am. Chem. Soc*. 2008; **130**: 2485–2492.
58. Shimizu Y and Azumi T. *J. Phys. Chem.* 1982; **86**: 22–26.
59. Geddes CD and Lakowicz JR. *J. Fluoresc*. 2002; **12**: 121–129.
60. Kubheka G, Uddin I, Amuhaya E, Mack J and Nyokong T. *J. Porphyrins Phthalocyanines* 2016; **20**: 1016–1024.